



Article

Polymer/Inorganic Hole Transport Layer for Low-Temperature-Processed Perovskite Solar Cells

Neda Irannejad ^{1,†}, Narges Yaghoobi Nia ^{2,†}, Siavash Adhami ³ , Enrico Lamanna ²,
Behzad Rezaei ^{1,*} and Aldo Di Carlo ^{2,4,*} 

¹ Chemistry Department, Isfahan University of Technology, Isfahan 84156-83111, Iran; neda.irannejad.69@gmail.com

² Centre for Hybrid and Organic Solar Energy (CHOSE), University of Rome Tor Vergata, 00133 Rome, Italy; yaghoobi.nia@ing.uniroma2.it (N.Y.N.); enrico.lamanna@uniroma2.it (E.L.)

³ Materials Engineering Department, Isfahan University of Technology, Isfahan 84156-83111, Iran; adhami@gmail.com

⁴ L.A.S.E.–Laboratory for Advanced Solar Energy, National University of Science and Technology “MISiS”, Leninskiy prospect 6, 119049 Moscow, Russia

* Correspondence: rezaei@cc.iut.ac.ir (B.R.); aldo.dicarlo@uniroma2.it (A.D.C.)

† The authors contributed equally to this work.

Received: 8 March 2020; Accepted: 14 April 2020; Published: 20 April 2020



Abstract: In the search for improvements in perovskite solar cells (PSCs), several different aspects are currently being addressed, including an increase in the stability and a reduction in the hysteresis. Both are mainly achieved by improving the cell structure, employing new materials or novel cell arrangements. We introduce a hysteresis-free low-temperature planar PSC, composed of a poly(3-hexylthiophene) (P3HT)/CuSCN bilayer as a hole transport layer (HTL) and a mixed cation perovskite absorber. Proper adjustment of the precursor concentration and thickness of the HTL led to a homogeneous and dense HTL on the perovskite layer. This strategy not only eliminated the hysteresis of the photocurrent, but also permitted power conversion efficiencies exceeding 15.3%. The P3HT/CuSCN bilayer strategy markedly improved the life span and stability of the non-encapsulated PSCs under atmospheric conditions and accelerated thermal stress. The device retained more than 80% of its initial efficiency after 100 h (60% after 500 h) of continuous thermal stress under ambient conditions. The performance and durability of the PSCs employing a polymer/inorganic bilayer as the HTL are improved mainly due to restraining perovskite ions, metals, and halides migration, emphasizing the pivotal role that can be played by the interface in the perovskite-additive hole transport materials (HTM) stack.

Keywords: interface; CuSCN; bilayer; poly(3-hexylthiophene); stability

1. Introduction

Halide perovskite solar cells (PSCs) have become one of the most investigated research topics in the renewable and sustainable energy community, owing to their effectiveness and high-power conversion efficiency (PCE) [1], recently reaching more than 25% [2].

The halide perovskite used for photovoltaics has a typical AMX_3 crystal structure, where A is a monovalent cation, such as Cs^+ , Rb^+ , $CH_3NH_3^+$, $NH_2CH = NH_2^+$, $CH_3CH_2NH_3^+$; $M = Pb_2^+$, Sn_2^+ ; and X is a halide, such as Cl^- , Br^- or I^- [3]. At the same time, employing a mixed-cation and mixed-halide perovskite composition can dramatically improve the performance and stability of PSCs [4,5].

In a typical PSC, the perovskite layer is deposited between a metal oxide electron transport layer (ETL), with either a mesoporous or planar structure, and a hole-transport layer (HTL). Several hole

transport materials (HTMs) have been considered so far, providing different final efficiencies, such as: (i) 2,2,7,7-tetrakis(N,N-di-p-methoxyphenylamine)-9,9-spirobifluorene (Spiro-OMeTAD) with a PCE of 22% [6]; (ii), poly(triarylamine) (PTAA) with a PCE of 20% [7]; (iii) poly(3,4-ethylenedioxythiophene):polystyrenesulfonate (PEDOT:PSS) with a PCE of 15% [8]; and iv) P3HT with PCE reaching 19.25% [9].

There are, however, several limitations in using these kinds of materials, such as excessive price, inefficient electron-blocking capability, and low chemical stability [10]. In this respect, inorganic HTLs seem to be a convincing alternative, with materials such as NiO [11], CuI [12,13] or CuSCN [14] being potential candidates.

CuSCN is a p-type inorganic semiconductor with a wide bandgap (3.4–3.9 eV) [15], high hole mobility, well-aligned work function [16], good thermal stability, high optical transparency and attractive mechanical properties [17,18]. The collection of the impressive physical and chemical properties, together with its low cost and commercial availability, has made CuSCN a very suitable material to be employed as an HTL. A PCE of more than 20% has been reported for PSCs with a conventional mesostructure TiO₂ ETL and CuSCN-reduced graphene oxide (rGO) HTL [19]. However, for planar n-i-p structures, using the atomic layer deposited TiO₂ ETL and CuSCN HTL, a maximum PCE of 12.7% has been achieved so far [20]. In order to improve the open-circuit voltage in CuSCN-based PSCs, various functional molecules have been introduced between the perovskite layer and copper on the surface of CH₃NH₃PbI₃ layers to passivate the defects and improve the contact between the MAPbI₃ and CuSCN layers [21]. Inorganic HTMs can be used in their original form without additives (which are commonly used in polymers or small molecules), leading to a significant improvement in the stability of solar cells [22–24]. In some cases, to overcome the instability problems, double-layer HTMs, such as CuSCN/Spiro-OMeTAD have been considered [21–23].

ETL is also one of the key components of PSCs due to its important role in the interfacial electron extraction and the final photovoltaic performance [24–27]. Planar structures of PSCs, in both regular n-i-p and inverted p-i-n stacks, have been widely explored due to the simple manufacturing process at low temperature and excellent device performance [28]. In the n-i-p PSC configuration, TiO₂ has been used extensively because of the favorable alignment to the conduction band of the perovskite absorber [29]. On the other hand, the high processing temperature (thermal annealing at 500–600 °C) [30], low electron mobility and strong photocatalytic activity represent severe drawbacks which restrict the use of TiO₂ [31]. It is worth noting that a high current–voltage hysteresis is observed when employing the mesoporous TiO₂ ETL [32,33]. It is very likely for this phenomenon to happen when the charge accumulation is induced by ion migration through the perovskite layer [34,35]. However, when the electronic contacts are optimized and the accumulated charges are well extracted, the hysteresis will be minimized or completely eliminated [36].

Different approaches have been adopted to overcome this problem. Fullerene and its derivatives have been used as an interface passivator [37], causing a significant decrement of hysteresis by improving the electron transfer process. Another approach was based on the use of metal oxides and transition metals, such as ZnO [38], In₂O₃ [39], SnO₂ [40], ZnS, CdS and CdSe [41,42], and [SiW₁₁O₃₉]⁸⁻ polyoxometalate [27] as suitable alternative ETLs to TiO₂. While the use of ZnO (with a PCE of 19%) has severely restricted its development because of thermal instability [43], SnO₂ appears to be a promising choice [44].

SnO₂ has high conductivity and electron mobility higher than that of TiO₂ by two orders of magnitude, appropriate energy levels (a wide bandgap ranging from 3.6 to 4.1 eV, which reduces the parasitic absorption caused by the ETL), high chemical/photo-stability and UV resistance [41–45], leading to its use as a semiconductor in various applications [46–48].

In this work, we present a hysteresis-free, high-efficiency planar PSC based on SnO₂ as the ETL and a P3HT/CuSCN bilayer as the HTL. CuSCN played a key role in improving the PCE of the perovskite solar cell due to its excellent transparency in the visible light spectrum range [49], high hole mobility [50], relatively good chemical stability [51] and a simple preparation process [52]. Triple-cation perovskite

was used as an absorber layer in our PSC, employing a one-step anti-solvent quenching method, which produced a lower surface roughness and smaller interface contact resistance when compared with the conventional two-step method [53]. After the final adjustment and optimization, a PCE of 15.3% was obtained by employing a polymer/inorganic bilayer (P3HT/CuSCN) strategy. Moreover, the atmospheric life span and thermal stability of non-encapsulated PSCs were significantly improved in P3HT/CUSCN based devices.

2. Materials and Methods

The fabricated devices in this work were made from FTO/glass substrates (Pilkington, $8\Omega\text{ cm}^{-1}$, $25\text{ mm} \times 25\text{ mm}$), etched by a raster scanning laser (Nd:YVO₄ pulsed at 30 kHz average output power, $P = 10\text{ W}$). The patterned substrates were cleaned in an ultrasonic bath by using deionized water, acetone and 2-propanol solution for 10 min intervals each. Then FTO was kept under a UV lamp for 20 min, and the SnO₂ solution (SnCl₂·2H₂O, in ethanol, 23.5 mg mL^{-1}) was deposited on the patterned FTO as ETL by two-step spin coating: 500 rpm with an acceleration of 250 rpm/s (for 4 s), followed by 2000 rpm with an acceleration of 1000 rpm s⁻¹ for 20 s. The substrates were then annealed for 10 min at 100 °C, followed by 180 °C for 3 h.

Prior to perovskite deposition, SnO₂ substrates were kept under a UV lamp for 1 h and then immediately transferred to the glove-box. The “mixed perovskite” solution contained FAI (1 M), CsI (0.05 M), PbI₂ (1.1 M), MABr (0.2 M), and PbBr₂ (0.22 M) dissolved in anhydrous DMF:DMSO 4:1 (v:v), as reported by Saliba et al. [3].

The perovskite layer was deposited by a one-step anti-solvent quenching method; the spin coating was performed in two parts, first at a speed of 1000 rpm for 10 s with an acceleration of 250 rpm s⁻¹, followed by a second step at 6000 rpm for 20 s with 2000 rpm s⁻¹. Chlorobenzene was dripped by micropipette over the spinning substrate 7 s before the end of the latter. The samples were then annealed at 100 °C on a hot plate for 1 h.

Different concentrations of CuSCN solutions were prepared (15 mg mL^{-1} , 25 mg mL^{-1} in dipropyl sulfide). Then 15 mg CuSCN powder was easily dissolved in dipropyl sulfide solvent, while the dissolution of 25 mg CuSCN in the same solvent required double filtration, with a 0.22 μm PTFE filter, followed by 1 h at 100 °C to obtain a clear solution, and finally the cold solution was spin-coated at 6000 rpm for 45 s. The substrates were then kept at 100 °C for 10 min to remove any remaining solvent, and another layer of CuSCN was deposited on top of the previous one and annealed for 10 min at 100 °C. In order to improve the stability of the fabricated PSCs to withstand 85 °C thermal cycling, a P3HT (124 kDa MW) in chlorobenzene solution was prepared following a previously reported procedure [54,55]. The P3HT layer was applied below and above the CuSCN by dynamic deposition following the same procedure as for the CuSCN layer, but without the final annealing step. At the end, 100 nm Au was deposited using thermal evaporation in a high vacuum chamber (10^{-6} mbar). All coating and fabrication steps were performed in a glovebox, except for the SnO₂ deposition. Figure 1 shows a schematic overview of the sample preparation process.

The morphology and the grain size of SnO₂, perovskite and HTM layers were investigated by field emission scanning electron microscopy (FE-SEM, HITACHI (S-4160)). The UV-Vis spectra were obtained by using a BLACK-Comet UV-Vis spectrometer (Dymax EC-5000 lamp, with irradiance power of 225 mWcm^{-2}) [56]. Dark J-V measurement and the photocurrent-voltage measurements of the devices were performed using a solar simulator (ABET Sun 2000, class A) under one-sun illumination conditions AM 1.5 (100 mWcm^{-2}), calibrated with a certified reference Si cell (RERA Solutions RR-1002). The electrochemical impedance spectroscopy (EIS) measurements were performed with an Eco-ChemieAutolab PGSTAT 302N electrochemical workstation controlled with NOVA software in the frequency range of 0.01 to 100 kHz, under 100 mWcm^{-2} solar simulator at a bias voltage ranging from 0.7 to 1.0 V.

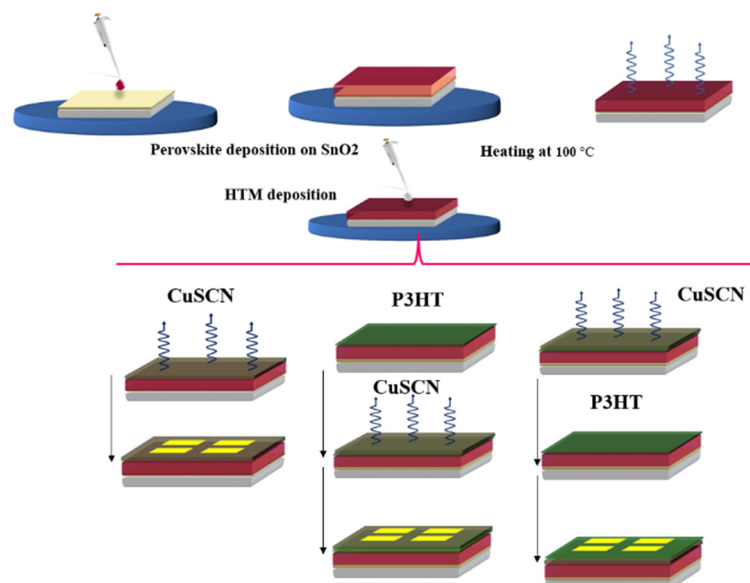


Figure 1. Schematic overview of the fabrication process for different types of perovskite solar cells (PSCs).

3. Results

The optical properties of the HTM on the perovskite layer were investigated by UV–Vis absorption spectroscopy (Figure 2). The absorption edge for all types of samples was observed at 750 nm, as expected. For the sample with P3HT, a clear onset of the P3HT absorption around 650 nm was observed [57].

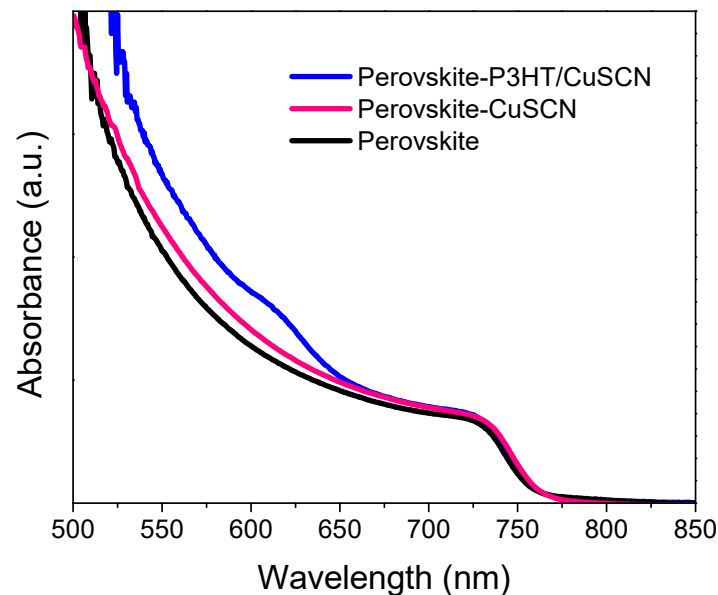


Figure 2. UV–Vis absorption spectra of perovskite and different HTMs on the perovskite layer.

The photovoltaic performance of the fabricated PSCs was evaluated under simulated sun AM 1.5 G (100 mWcm^{-2}). The PV parameters obtained from the J–V curves of the devices are shown in Figure 3 and Figure S1 of the Supporting Materials. The corresponding results are also given in Table 1.

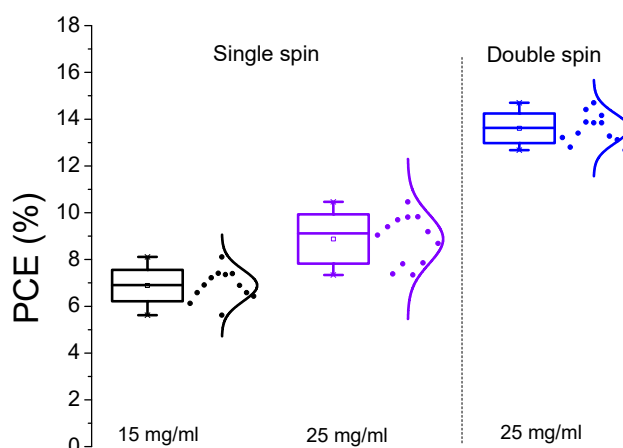


Figure 3. Power Conversion Efficiencies (PCEs) of SnO₂/Perovskite/CuSCN/Au-based devices (in two different concentrations of 15 and 25 mg mL⁻¹ of CuSCN in dipropyl sulfide). The first two sets are related to single-spin deposition (thickness of the CuSCN = 60 nm), while the last set considers a double-spin coating CuSCN deposition (thickness = 90 nm). PSC with an active area of 0.09 cm².

Table 1. Photovoltaic characteristics of the most efficient device of the set. The average ± standard deviations are reported between brackets.

SnO ₂ /Perovskite/CuSCN/Au Device	J _{sc} (mA cm ⁻²)	V _{oc} (V)	FF *	H **%
15 mg mL ⁻¹ CuSCN (single-spin)	20.46 (19.6 ± 0.9)	0.85 (0.77 ± 0.08)	0.48 (0.46 ± 0.02)	8.2 (6.7 ± 1.2)
25 mg mL ⁻¹ CuSCN (single-spin)	20.15 (20.0 ± 0.1)	0.93 (0.92 ± 0.01)	0.56 (0.51 ± 0.05)	10.5 (8.8 ± 1.7)
25 mg mL ⁻¹ CuSCN (double-spin)	20.87 (20.4 ± 0.4)	1.02 (0.97 ± 0.05)	0.69 (0.68 ± 0.01)	14.7 (13.2 ± 1.5)

* Fill factor = $P_{max}/(I_{sc} \times V_{oc})$. ** Power conversion efficiency = $(I_{sc} \times V_{oc} \times FF/100) \times 100\%$.

The concentration of the precursor solution and the thickness of the HTL seemed to play a key role in the performance assessment of the PSCs. Higher PCE results were obtained with 25 mg mL⁻¹ CuSCN in dipropyl sulfide.

Increasing the thickness of the CuSCN layer up to 90 nm, achieved with a double-spin coating, improved the maximum (average) efficiency up to 14.7% (13.2%), as reported in Figure 3 and Figure S1, respectively. This significant improvement is essentially related to the increase in open-circuit voltage (V_{oc}) and fill factor (FF), as shown in Table 1. Based on the results, by increasing the thickness of the CuSCN layer, the V_{oc} was significantly increased. This improvement can be attributed to a better hole extraction due to a reduction in recombination phenomena. On the other hand, a significant improvement in FF implies a reduction in contact resistance and improved charge transfer processes.

As mentioned before, one of the most important parameters of PSC devices is hysteresis, which is normally investigated by comparing the forward and backward J-V scan. Figure 4A reports the measured forward and reverse J-V characteristics for the P3HT/CuSCN-based PSC. A reverse PCE of 15.3% (J_{sc} = 21.35 mA, a V_{oc} = 1.00 V, and FF = 0.72%) was achieved, compared with a 14.7% (J_{sc} = 21.06 mA, a V_{oc} = 1.00 V, and FF = 0.70%) of the forward measurement. The very limited J-V hysteresis of the P3HT/CuSCN/Au-based PSC is attributed to the improved electronic connection of the layers and a lower accumulation of charges in the structure [25].

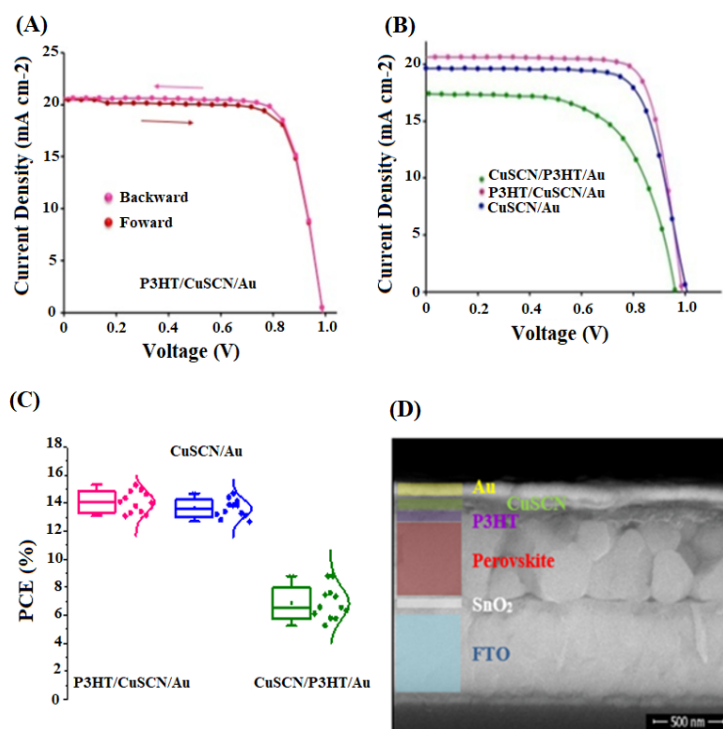


Figure 4. (A) J-V characteristics of P3HT/CuSCN-based PSC (CuSCN layer was deposited by a double-spin of 25 mg mL^{-1} in dipropyl sulfide solution); (B) J-V curves; (C) the PCEs of SnO_2 /perovskite/HTM/Au-based devices (with CuSCN, P3HT/CuSCN, and CuSCN/P3HT as an HTL) with an active area of 0.09 cm^2 ; (D) cross-sectional SEM micrographs of the SnO_2 -based perovskite solar cell with P3HT/CuSCN as a hole transport layer.

The J-V plots for the PSCs with the different situations of the P3HT layer (perovskite-HTL and HTL-Au interfaces) are shown in Figure 4B. The statistical PCEs are shown in Figure 4C. Furthermore, the FE-SEM cross-section image from the P3HT/CuSCN-based device is also presented in Figure 4D.

The PV parameters obtained from the J-V curve indicate that the P3HT/CuSCN/Au-based device (Figure 4C and Figure S2) showed a better performance (PCE = 15.3%), compared with the CuSCN/P3HT/Au-based device (PCE = 8.8%).

A summary of the statistical analysis of PV parameters, extracted from J-V curves for 12 independent devices, are given in Figure 4C and Figure S2, while max (average \pm standard deviation) PV parameters are reported in Table 2.

Table 2. Photovoltaic characteristics of SnO_2 /perovskite/HTM/Au devices. Performances of the best efficiencies are presented, with average values and standard deviation.

PSCs	$J_{sc} (\text{mA cm}^{-2})$	$V_{oc} (\text{V})$	FF	$\eta\%$
SnO_2 /Perovskite/CuSCN/Au	20.87 (20.4 ± 0.4)	1.02 (0.97 ± 0.05)	0.69 (0.68 ± 0.01)	14.7 (13.2 ± 1.5)
SnO_2 /Perovskite/P3HT/CuSCN/Au	21.35 (21.2 ± 0.3)	1.00 (0.8 ± 0.2)	0.72 (0.67 ± 0.03)	15.3 (14.54 ± 0.75)
SnO_2 /Perovskite/CuSCN/P3HT/Au	17.73 (16.90 ± 0.8)	0.96 (0.89 ± 0.07)	0.52 (0.51 ± 0.01)	8.8 (6.89 ± 1.9)

The stability of the non-encapsulated cells, under environmental and thermal conditions, are shown in Figure 5A,B, respectively. The atmospheric shelf-life of PSCs with a P3HT interlayer (Figure 5A) was longer than that with only CuSCN. As shown in Figure 5B, the thermal stability of the P3HT/CuSCN/Au structure turned out to be several times better compared with the devices having other arrangements. Planar PSCs using the CuSCN HTL or the CuSCN/P3HT HTL rapidly lose their initial efficiency against

85 °C thermal stress, mainly due to the interaction between CuSCN and perovskite. This phenomenon could be related to a structural change of perovskite surface upon heating at 85 °C [58], which could be accelerated by Cu(II) ions through a reaction with halide ions and form copper halide defects. Furthermore, due to the constraints on the CuSCN precursor solvent (requirement of polar solvents), the interaction of such solvents with perovskite surface during deposition of HTM leads to increased defects on the perovskite layer and accelerates the thermal decomposition. On the other hand, by using the P3HT/CuSCN bilayer structure as the HTL, the device could retain more than 80% of its initial efficiency after 100 h of continuous thermal stress. The positive effect of the P3HT layer could be attributed to: (i) polymeric barrier against diffusion of mobile ions of perovskite layer to the back contact [59]; (ii) passivation of perovskite surface against polar solvents of the CuSCN precursor; (iii) reduction in the metal diffusion [59,60]. In particular, the robust hydrophobic nature of P3HT [61], achieved reasonable passivation against atmospheric water and oxygen.

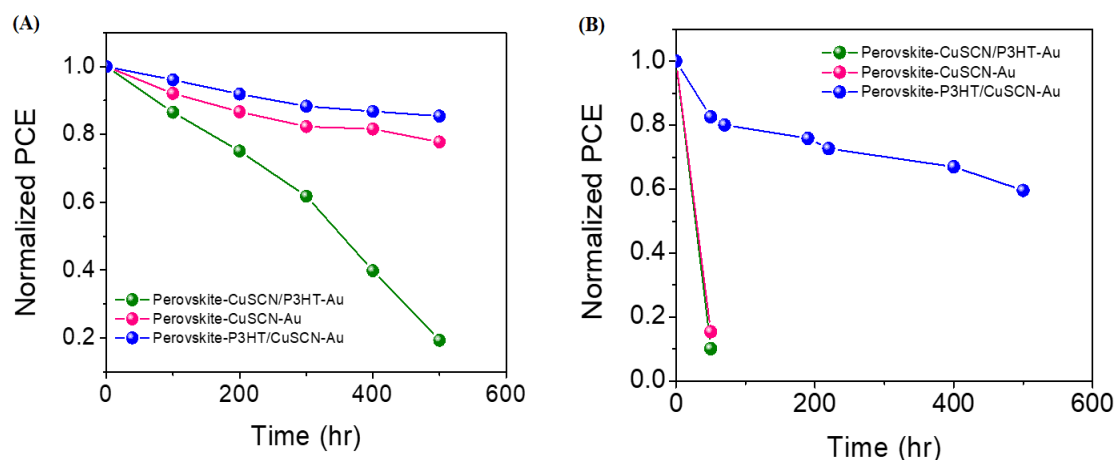


Figure 5. Stability of the non-encapsulated SnO₂/perovskite/HTM/Au-devices (with CuSCN, P3HT/CuSCN, CuSCN/P3HT as HTL), examined at (A) ambient conditions and (B) under thermal stress at 85 °C.

To study the intrinsic mechanism ruling the performances of PSCs made with different HTLs, we performed a series of experiments to identify charge recombination and transfer. Regarding the evaluation of the recombination process in the fabricated devices (CuSCN and P3HT/CuSCN as HTL), we used J-V measurement under dark conditions and corresponding Tafel plots as shown in Figure 6A. Generally, the leakage current of the P3HT/CuSCN was one order lower than that for the device with CuSCN only. Although both devices showed almost the same shunt resistance and recombination in the depletion layer, the main difference arose from recombination in the neutral layer, which was mainly governed by trap-assisted recombination mechanisms.

When the applied bias reached ~0.8 V, the device containing P3HT/CuSCN shows a sharp trap filling behavior that evidences very high trap-assisted recombination resistance. Furthermore, despite the addition of an extra (P3HT) layer, there was no sign of increment in the depletion layer's recombination, which could be attributed to the intrinsic fast carrier mobility of P3HT and better coverage of the perovskite interface with P3HT.

The EIS was also carried out under dark conditions at different bias potentials to better define the electron transport/recombination process within the PSC. The semicircle in the Nyquist plots (Figure S4) was related to the impedance of the free charge carriers' recombination at the perovskite/HTM layer (R_{rec}). The highest R_{rec} indicated the lowest recombination process because of the longer free charge carriers' lifetime and their proper collection [55]. Figure 6B evidences that the recombination resistance significantly increased in the presence of a P3HT/CuSCN/Au-based PSCs, in excess of two orders of magnitude. This improvement could be associated with the uniform coating of the P3HT/CuSCN layer as well as the supporting role of the P3HT layer in blocking the diffusion of ions.

In order to calculate the lifetimes of the free charge carriers, constant phase elements (CPE) were extracted from the Nyquist curves (Figure 6). The highest lifetime was obtained for P3HT/CuSCN/Au-based under intermediate voltages, compared with those cells having different arrangements. This is in full agreement with the data obtained from dark J-V and EIS analysis (Figure 6).

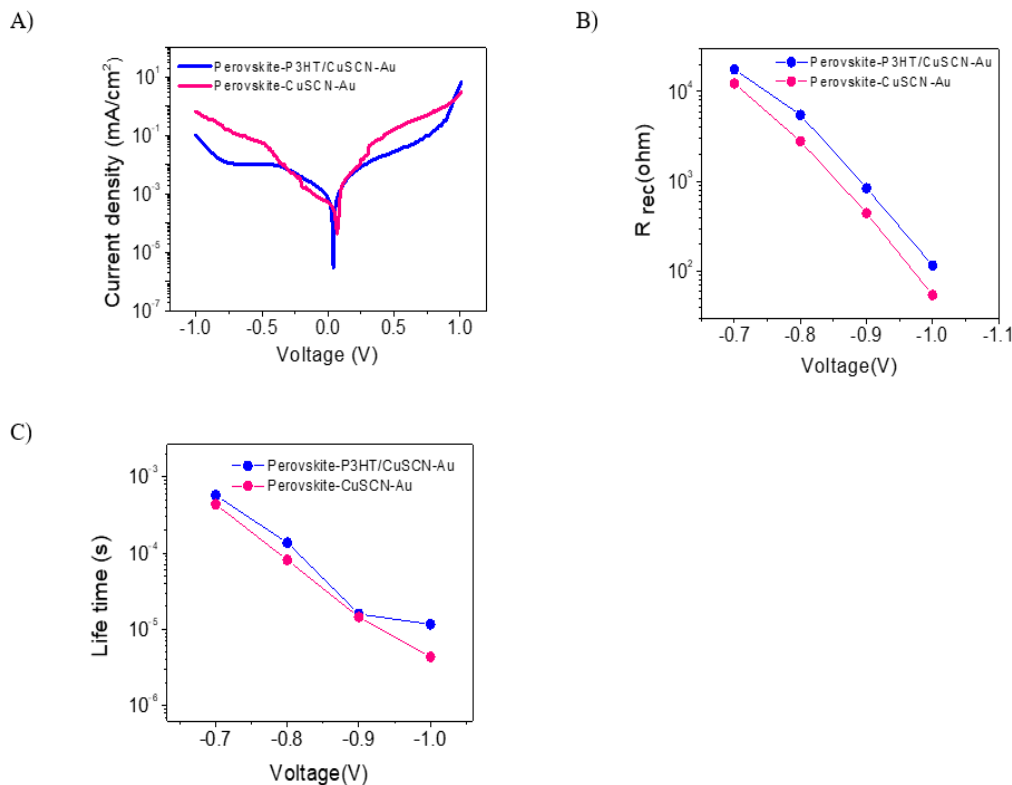


Figure 6. (A) Dark J-V plots; (B) recombination resistance/charge transfer interfacial resistance (R_{rec}) extracted from electrochemical impedance spectroscopy (EIS) under different bias potential under dark conditions; (C) effective carrier lifetime calculated as the product between R_{rec} and the chemical capacitance (c_{μ}) of SnO_2 /perovskite/HTM/Au-based devices (with CuSCN, P3HT/CuSCN, P3HT as an HTL) with an active area of 0.09 cm^2 .

4. Conclusions

A hysteresis-free planar n-i-p perovskite solar cell with a PCE of $\sim 15.3\%$ was developed with a P3HT/CuSCN bilayer as an HTL. The designed structure exhibited better performance by enhancing the electron transfer rate and reducing the recombination processes with respect to the typical CuSCN layer. Therefore, the present work can be considered as an effective and promising way to realize hysteresis-free SnO_2 -based planar perovskite solar cells through the use of P3HT/CuSCN as a cost-effective and suitable HTL alternative to conventional materials, such as Spiro-OMeTAD. It was further proved that the long-term stability of PSCs can be significantly increased by using P3HT as an interlayer between the perovskite and CuSCN. By employing this bilayer strategy, PSCs can maintain more than 80% of their initial PCE after 100 h under the continuous thermal stress conditions at 85°C . The performance and durability of the PSCs were well improved and the hysteresis effect was prevented by restraining the perovskite ions, metals and halides migration, emphasizing the pivotal role that can be played by the interface in the perovskite-additive-HTM stack.

Supplementary Materials: The following are available online at <http://www.mdpi.com/1996-1073/13/8/2059/s1>, Figure S1: Photovoltaic parameters of SnO_2 /Perovskite/CuSCN/Au based devices (with single and double spin coating of 25 mg mL^{-1} of CuSCN in dipropyl sulfide). The first two sets are related to single spin deposition while the set consider a double spin coating CuSCN deposition PSC with an active area of 0.09 cm^2 , Figure S2: Photovoltaic parameters of SnO_2 /perovskite/HTM/Au based devices (with CuSCN, P3HT/CuSCN, CuSCN/P3HT as

an HTL) with an illumination area of 0.09 cm², Figure S3: Photovoltaic parameters of SnO₂/Perovskite/CuSCN/Au, SnO₂/Perovskite/P3HT/CuSCN/Au and SnO₂/Perovskite/CuSCN/P3HT/Au under (A) environmental and (B) thermal conditions with an illumination area of 0.09 cm², Figure S4: Nyquist plot and equivalent circuit of SnO₂/Perovskite/CuSCN/Au, SnO₂/Perovskite/P3HT/CuSCN/Au at different bias voltage.

Author Contributions: Conceptualization, N.Y.N. and A.D.C.; methodology, N.Y.N.; software, N.I. and N.Y.N.; validation, N.I., N.Y.N. and E.L.; formal analysis, N.I., N.Y.N., A.D.C. and S.A.; investigation, N.I., N.Y.N. and E.L.; resources, A.D.C.; data curation, N.I., N.Y.N. and A.D.C.; writing—original draft preparation, N.I.; writing—review and editing, N.Y.N., E.L., A.D.C., and B.R.; visualization, N.Y.N. and A.D.C.; supervision, N.Y.N.; project administration, A.D.C.; funding acquisition, A.D.C. All authors have read and agreed to the published version of the manuscript.

Funding: This research was funded by Italian Ministry of Economic Development in the framework of the Operating Agreement with ENEA for Research on the Electric System (Accordo di Programma 2019–2021) and the European Union's Horizon 2020 Framework Program for funding Research and Innovation under grant agreement no. 764047 (ESPRESSO).

Acknowledgments: CHOSE group thanks the Italian Ministry of Economic Development in the framework of the Operating Agreement with ENEA for Research on the Electric System for supporting this work. The IUT group greatly acknowledges the Ministry of Science, Research and Technology of I.R. Iran, Iran National Science Foundation (INSF), Iran National Elites Foundation (INEF) and A. Kermanpur for their support. ADC gratefully acknowledges the financial support of the Ministry of Education and Science of the Russian Federation in the framework of MegaGrant N° 075-15-2019-872 (14.Y26.31.0027/074-02-2018-327).

Conflicts of Interest: The authors declare no conflicts of interest. The funders had no role in the design of the study; in the collection, analyses, or interpretation of data; in the writing of the manuscript, or in the decision to publish the results.

References

1. Djurišić, A.B.; Liu, F.Z.; Tam, H.W.; Wong, M.K.; Ng, A.; Surya, C.; Chen, W.; He, Z.B. Perovskite solar cells—An overview of critical issues. *Prog. Quantum Electron.* **2017**, *53*, 1–37. [CrossRef]
2. Best Research-Cell Efficiency Chart. Available online: <https://www.nrel.gov/pv/cell-efficiency.html> (accessed on 13 April 2020).
3. Saliba, M.; Matsui, T.; Seo, J.-Y.; Domanski, K.; Correa-Baena, J.-P.; Nazeeruddin, M.K.; Zakeeruddin, S.M.; Tress, W.; Abate, A.; Hagfeldt, A.; et al. Cesium-containing triple cation perovskite solar cells: Improved stability, reproducibility and high efficiency. *Energy Environ. Sci.* **2016**, *9*, 1989–1997. [CrossRef] [PubMed]
4. Chen, L.; Tan, Y.-Y.; Chen, Z.-X.; Wang, T.; Hu, S.; Nan, Z.-A.; Xie, L.-Q.; Hui, Y.; Huang, J.-X.; Zhan, C.; et al. Toward Long-Term Stability: Single-Crystal Alloys of Cesium-Containing Mixed Cation and Mixed Halide Perovskite. *J. Am. Chem. Soc.* **2019**, *141*, 1665–1671. [CrossRef] [PubMed]
5. Yaghoobi, N.; Giordano, F.; Zendejdel, M.; Cinà, L.; Palma, A.L.; Medaglia, P.G.; Zakeeruddin, S.M.; Grätzel, M.; Di Carlo, A. Solution-based heteroepitaxial growth of stable mixed cation/anion hybrid perovskite thin film under ambient condition via a scalable crystal engineering approach. *Nano Energy* **2020**, *69*, 104441. [CrossRef]
6. Hawash, Z.; Ono, L.K.; Qi, Y. Recent Advances in Spiro-MeOTAD Hole Transport Material and Its Applications in Organic-Inorganic Halide Perovskite Solar Cells. *Adv. Mater. Interfaces* **2018**, *5*, 1700623. [CrossRef]
7. Zhang, F.; Lu, H.; Tong, J.; Berry, J.J.; Beard, M.C.; Zhu, K. Advances in Two-Dimensional Organic-Inorganic Hybrid Perovskites. *Energy Environ. Sci.* **2020**, *13*, 1154–1186. [CrossRef]
8. Lee, K.; Yu, H.; Lee, J.W.; Oh, J.; Bae, S.; Kim, S.K.; Jang, J. Efficient and moisture-resistant hole transport layer for inverted perovskite solar cells using solution-processed polyaniline. *J. Mater. Chem. C* **2018**, *6*, 6250–6256. [CrossRef]
9. Yaghoobi, N.; Lamanna, E.; Zendejdel, M.; Palma, A.L.; Zurlo, F.; Castriotta, L.A.; Di Carlo, A. Doping Strategy for Efficient and Stable Triple Cation Hybrid Perovskite Solar Cells and Module Based on Poly(3-hexylthiophene) Hole Transport Layer. *Small* **2019**, *15*, 1904399. [CrossRef]
10. Calio, L.; Kazim, S.; Grätzel, M.; Ahmad, S. Hole-Transport Materials for Perovskite Solar Cells. *Angew. Chem. Int. Ed.* **2016**, *55*, 14522–14545. [CrossRef]
11. Christians, J.A.; Fung, R.C.M.; Kamat, P.V. An Inorganic Hole Conductor for Organo-Lead Halide Perovskite Solar Cells. Improved Hole Conductivity with Copper Iodide. *J. Am. Chem. Soc.* **2014**, *136*, 758–764. [CrossRef]

12. Chavhan, S.; Miguel, O.; Grande, H.-J.; Gonzalez-Pedro, V.; Sánchez, R.S.; Barea, E.M.; Mora-Seró, I.; Tena-Zaera, R. Organo-metal halide perovskite-based solar cells with CuSCN as the inorganic hole selective contact. *J. Mater. Chem. A* **2014**, *2*, 12754–12760. [[CrossRef](#)]
13. Sepalage, G.A.; Meyer, S.; Pascoe, A.; Scully, A.D.; Huang, F.; Bach, U.; Cheng, Y.-B.; Spiccia, L. Copper(I) Iodide as Hole-Conductor in Planar Perovskite Solar Cells: Probing the Origin of J–V Hysteresis. *Adv. Funct. Mater.* **2015**, *25*, 5650–5661. [[CrossRef](#)]
14. Wijeyasinghe, N.; Regoutz, A.; Eisner, F.; Du, T.; Tsetseris, L.; Lin, Y.-H.; Faber, H.; Pattanasattayavong, P.; Li, J.; Yan, F.; et al. Copper(I) Thiocyanate (CuSCN) Hole-Transport Layers Processed from Aqueous Precursor Solutions and Their Application in Thin-Film Transistors and Highly Efficient Organic and Organometal Halide Perovskite Solar Cells. *Adv. Funct. Mater.* **2017**, *27*, 1701818. [[CrossRef](#)]
15. Wijeyasinghe, N.; Anthopoulos, T.D. Copper(I) thiocyanate (CuSCN) as a hole-transport material for large-area opto/electronics. *Semicond. Sci. Technol.* **2015**, *30*, 104002. [[CrossRef](#)]
16. Chaudhary, N.; Chaudhary, R.; Kesari, J.P.; Patra, A.; Chand, S. Copper thiocyanate (CuSCN): An efficient solution-processable hole transporting layer in organic solar cells. *J. Mater. Chem. C* **2015**, *3*, 11886–11892. [[CrossRef](#)]
17. Nam-GyuPark Perovskite solar cells: An emerging photovoltaic technology. *Mater. Today* **2015**, *18*, 65–72. [[CrossRef](#)]
18. Zhao, K.; Munir, R.; Yan, B.; Yang, Y.; Kim, T.; Amassian, A. Solution-processed inorganic copper(i) thiocyanate (CuSCN) hole transporting layers for efficient p-i-n perovskite solar cells. *J. Mater. Chem. A* **2015**, *3*, 20554–20559. [[CrossRef](#)]
19. Arora, N.; Dar, M.I.; Hinderhofer, A.; Pellet, N.; Schreiber, F.; Zakeeruddin, S.M.; Grätzel, M. Perovskite solar cells with CuSCN hole extraction layers yield stabilized efficiencies greater than 20%. *Science* **2017**, *358*, 768–771. [[CrossRef](#)]
20. Fan, L.; Li, Y.; Yao, X.; Ding, Y.; Zhao, S.; Shi, B.; Wei, C.; Zhang, D.; Li, B.; Wang, G.; et al. Delayed Annealing Treatment for High-Quality CuSCN: Exploring Its Impact on Bifacial Semitransparent n-i-p Planar Perovskite Solar Cells. *ACS Appl. Energy Mater.* **2018**, *1*, 1575–1584. [[CrossRef](#)]
21. Yang, I.S.; Lee, S.; Choi, J.; Jung, M.T.; Kim, J.; Lee, W.H.I. Enhancement of Open Circuit Voltage for the CuSCN-employed Perovskite Solar Cells by Controlling Perovskite/CuSCN Interface with Functional Molecules. *J. Mater. Chem. A* **2019**, *7*, 6028–6037. [[CrossRef](#)]
22. Premalal, E.V.A.; Kumara, G.R.R.A.; Rajapakse, R.M.G.; Shimomura, M.; Murakami, K.; Konno, A. Tuning chemistry of CuSCN to enhance the performance of TiO₂/N719/CuSCN all-solid-state dye-sensitized solar cell. *Chem. Commun.* **2010**, *46*, 3360–3362. [[CrossRef](#)] [[PubMed](#)]
23. O'Regan, B.; Schwartz, D.T. Large Enhancement in Photocurrent Efficiency Caused by UV Illumination of the Dye-Sensitized Heterojunction TiO₂/RuLL'NCS/CuSCN: Initiation and Potential Mechanisms. *Chem. Mater.* **1998**, *10*, 1501–1509. [[CrossRef](#)]
24. Kumara, G.R.R.; Konno, A.; Senadeera, G.K.; Jayaweera, P.V.; De Silva, D.B.R.; Tennakone, K. Dye-sensitized solar cell with the hole collector p-CuSCN deposited from a solution in n-propyl sulphide. *Sol. Energy Mater. Sol. Cells* **2001**, *69*, 195–199. [[CrossRef](#)]
25. Li, Q.; Zhao, Y.Y.; Fu, R.; Zhou, W.; Zhao, Y.Y.; Lin, F.; Liu, S.; Yu, D.; Zhao, Q. Enhanced long-term stability of perovskite solar cells using a double-layer hole transport material. *J. Mater. Chem. A* **2017**, *5*, 14881–14886. [[CrossRef](#)]
26. Yang, G.; Chen, C.; Yao, F.; Chen, Z.; Zhang, Q.; Zheng, X.; Ma, J.; Lei, H.; Qin, P.; Xiong, L.; et al. Effective Carrier-Concentration Tuning of SnO₂ Quantum Dot Electron-Selective Layers for High-Performance Planar Perovskite Solar Cells. *Adv. Mater.* **2018**, *30*, 1706023. [[CrossRef](#)] [[PubMed](#)]
27. Sardashti, M.K.; Zendehtel, M.; Nia, N.Y.; Karimian, D.; Sheikhi, M. High Efficiency MAPbI₃ Perovskite Solar Cell Using a Pure Thin Film of Polyoxometalate as Scaffold Layer. *ChemSusChem* **2017**, *10*, 3773–3779. [[CrossRef](#)]
28. Lee, Y.; Lee, S.; Seo, G.; Paek, S.; Cho, K.T.; Huckaba, A.J.; Calizzi, M.; Choi, D.; Park, J.-S.; Lee, D.; et al. Efficient Planar Perovskite Solar Cells Using Passivated Tin Oxide as an Electron Transport Layer. *Adv. Sci.* **2018**, *5*, 1800130. [[CrossRef](#)]
29. Heo, J.H.; Han, H.J.; Kim, D.; Ahn, T.K.; Im, S.H. Hysteresis-less inverted CH₃NH₃PbI₃ planar perovskite hybrid solar cells with 18.1% power conversion efficiency. *Energy Environ. Sci.* **2015**, *8*, 1602–1608. [[CrossRef](#)]

30. Huang, Z.; Wang, D.; Wang, S.; Zhang, T. Highly Efficient and Stable MAPbI₃ Perovskite Solar Cell Induced by Regulated Nucleation and Ostwald Recrystallization. *Materials* **2018**, *11*, 778. [[CrossRef](#)]
31. El Harrad, L.; Bourais, I.; Mohammadi, H.; Amine, A. Recent Advances in Electrochemical Biosensors Based on Enzyme Inhibition for Clinical and Pharmaceutical Applications. *Sensors* **2018**, *18*, 164. [[CrossRef](#)]
32. Yoon, H.; Kang, S.M.; Lee, J.-K.; Choi, M. Hysteresis-free low-temperature-processed planar perovskite solar cells with 19.1% efficiency. *Energy Environ. Sci.* **2016**, *9*, 2262–2266. [[CrossRef](#)]
33. Zhao, Y.; Liang, C.; Zhang, H.; Li, D.; Tian, D.; Li, G.; Jing, X.; Zhang, W.; Xiao, W.; Liu, Q.; et al. Anomalously large interface charge in polarity-switchable photovoltaic devices: An indication of mobile ions in organic–inorganic halide perovskites. *Energy Environ. Sci.* **2015**, *8*, 1256–1260. [[CrossRef](#)]
34. Tress, W.; Marinova, N.; Moehl, T.; Zakeeruddin, S.M.; Nazeeruddin, M.K.; Grätzel, M. Understanding the rate-dependent J–V hysteresis, slow time component, and aging in CH₃NH₃PbI₃ perovskite solar cells: The role of a compensated electric field. *Energy Environ. Sci.* **2015**, *8*, 995–1004. [[CrossRef](#)]
35. Jiang, Q.; Zhang, L.; Wang, H.; Yang, X.; Meng, J.; Liu, H.; Yin, Z.; Wu, J.; Zhang, X.; You, J. Enhanced electron extraction using SnO₂ for high-efficiency planar-structure HC(NH₂)₂PbI₃-based perovskite solar cells. *Nat. Energy* **2017**, *2*, 16177. [[CrossRef](#)]
36. Liu, D.; Kelly, T.L. Perovskite solar cells with a planar heterojunction structure prepared using room-temperature solution processing techniques. *Nat. Photonics* **2014**, *8*, 133–138. [[CrossRef](#)]
37. Wang, Y.-C.; Li, X.; Zhu, L.; Liu, X.; Zhang, W.; Fang, J. Efficient and Hysteresis-Free Perovskite Solar Cells Based on a Solution Processable Polar Fullerene Electron Transport Layer. *Adv. Energy Mater.* **2017**, *7*, 1701144. [[CrossRef](#)]
38. Abulikemu, M.; Neophytou, M.; Barbé, J.M.; Tietze, M.L.; El Labban, A.; Anjum, D.H.; Amassian, A.; McCulloch, I.; Del Gobbo, S. Microwave-synthesized tin oxide nanocrystals for low-temperature solution-processed planar junction organo-halide perovskite solar cells. *J. Mater. Chem. A* **2017**, *5*, 7759–7763. [[CrossRef](#)]
39. Hou, Y.; Chen, X.; Yang, S.; Zhong, Y.L.; Li, C.; Zhao, H.; Yang, H.G. Low-temperature processed In₂S₃ electron transport layer for efficient hybrid perovskite solar cells. *Nano Energy* **2017**, *36*, 102–109. [[CrossRef](#)]
40. Liu, J.; Gao, C.; Luo, L.; Ye, Q.; He, X.; Ouyang, L.; Guo, X.; Zhuang, D.; Liao, C.; Mei, J.; et al. Low-temperature, solution processed metal sulfide as an electron transport layer for efficient planar perovskite solar cells. *J. Mater. Chem. A* **2015**, *3*, 11750–11755. [[CrossRef](#)]
41. Ding, B.; Gao, L.; Liang, L.; Chu, Q.; Song, X.; Li, Y.; Yang, G.; Fan, B.; Wang, M.; Li, C.; et al. Facile and Scalable Fabrication of Highly Efficient Lead Iodide Perovskite Thin-Film Solar Cells in Air Using Gas Pump Method. *ACS Appl. Mater. Interfaces* **2016**, *8*, 20067–20073. [[CrossRef](#)]
42. Wang, L.; Fu, W.; Gu, Z.; Fan, C.; Yang, X.; Li, H.; Chen, H. Low temperature solution processed planar heterojunction perovskite solar cells with a CdSe nanocrystal as an electron transport/extraction layer. *J. Mater. Chem. C* **2014**, *2*, 9087–9090. [[CrossRef](#)]
43. Jung, K.-H.; Seo, J.-Y.; Lee, S.; Shin, H.; Park, N.-G. Solution-processed SnO₂ thin film for a hysteresis-free planar perovskite solar cell with a power conversion efficiency of 19.2%. *J. Mater. Chem. A* **2017**, *5*, 24790–24803. [[CrossRef](#)]
44. Song, J.; Zheng, E.; Bian, J.; Wang, X.-F.; Tian, W.; Sanehira, Y.; Miyasaka, T. Low-temperature SnO₂-based electron selective contact for efficient and stable perovskite solar cells. *J. Mater. Chem. A* **2015**, *3*, 10837–10844. [[CrossRef](#)]
45. Yu, H.; Yeom, H.-I.; Lee, J.W.; Lee, K.; Hwang, D.; Yun, J.; Ryu, J.; Lee, J.; Bae, S.; Kim, S.K.; et al. Superfast Room-Temperature Activation of SnO₂ Thin Films via Atmospheric Plasma Oxidation and their Application in Planar Perovskite Photovoltaics. *Adv. Mater.* **2018**, *30*, 1704825. [[CrossRef](#)] [[PubMed](#)]
46. Navazani, S.; Shokuhfar, A.; Hassanisadi, M.; Di Carlo, A.; Yaghoobi, N.; Agresti, A. A PdPt decorated SnO₂-rGO nanohybrid for high-performance resistive sensing of methane. *J. Taiwan Inst. Chem. Eng.* **2019**, *95*, 438–451. [[CrossRef](#)]
47. Habibi, M.H.; Mardani, M.; Habibi, M.; Zendehtdel, M. Enhanced photovoltage (Voc) of nano-structured zinc tin oxide (ZTO) working electrode prepared by a green hydrothermal route for dye-sensitized solar cell (DSSC). *J. Mater. Sci. Mater. Electron.* **2017**, *28*, 3789–3795. [[CrossRef](#)]
48. Kong, Z.; Liu, D.; Liu, X.; Fu, A.; Wang, Y.; Guo, P.; Li, H. One-Pot Decoration of Graphene with SnO₂ Nanocrystals by an Elevated Hydrothermal Process and Their Application as Anode Materials for Lithium Ion Batteries. *J. Nanosci. Nanotechnol.* **2019**, *19*, 850–858. [[CrossRef](#)]

49. Yuan, L.; Wang, Z.; Duan, R.; Huang, P.; Zhang, K.; Chen, Q.; Allam, N.K.; Zhou, Y.; Song, B.; Li, Y. Semi-transparent perovskite solar cells: Unveiling the trade-off between transparency and efficiency. *J. Mater. Chem. A* **2018**, *6*, 19696–19702. [[CrossRef](#)]
50. Murugadoss, G.; Kanda, H.; Tanaka, S.; Nishino, H.; Ito, S.; Imahoric, H.; Umeyama, T. An efficient electron transport material of tin oxide for planar structure perovskite solar cells. *J. Power Sour.* **2016**, *307*, 891–897. [[CrossRef](#)]
51. Tjep, N.H.; Ku, Z.; Fan, H.J. Recent Advances in Improving the Stability of Perovskite Solar Cells. *Adv. Energy Mater.* **2016**, *6*, 1501420. [[CrossRef](#)]
52. Ye, S.; Rao, H.; Yan, W.; Li, Y.; Sun, W.; Peng, H.; Liu, Z.; Bian, Z.; Li, Y.; Huang, C. A Strategy to Simplify the Preparation Process of Perovskite Solar Cells by Co-deposition of a Hole-Conductor and a Perovskite Layer. *Adv. Mater.* **2016**, *28*, 9648–9654. [[CrossRef](#)] [[PubMed](#)]
53. Petrus, M.L.; Schlipf, J.; Li, C.; Gujar, T.P.; Giesbrecht, N.; Müller-Buschbaum, P.; Thelakkat, M.; Bein, T.; Hüttner, S.; Docampo, P. Capturing the Sun: A Review of the Challenges and Perspectives of Perovskite Solar Cells. *Adv. Energy Mater.* **2018**, *8*, 1703396. [[CrossRef](#)]
54. Yaghoobi, N.; Matteocci, F.; Cina, L.; Di Carlo, A. High-Efficiency Perovskite Solar Cell Based on Poly(3-Hexylthiophene): Influence of Molecular Weight and Mesoscopic Scaffold Layer. *ChemSusChem* **2017**, *10*, 3854–3860.
55. Yaghoobi, N.; Zendejdel, M.; Cinà, L.; Matteocci, F.; Di Carlo, A. A crystal engineering approach for scalable perovskite solar cells and module fabrication: A full out of glove box procedure. *J. Mater. Chem. A* **2018**, *6*, 659–671. [[CrossRef](#)]
56. Calabrò, E.; Matteocci, F.; Palma, A.L.; Vesce, L.; Taheri, B.; Carlini, L.; Pis, I.; Nappini, S.; Dagar, J.; Battocchio, C.; et al. Low Temperature, Solution-processed Perovskite Solar Cells and Modules with an Aperture Area Efficiency of 11%. *Sol. Energy Mater. Sol. Cells* **2018**, *185*, 136–144. [[CrossRef](#)]
57. Rahimi, K.; Botiz, I.; Agumba, J.O.; Motamen, S.; Stingelin, N.; Reiter, G. Light absorption of poly(3-hexylthiophene) single crystals. *RSC Adv.* **2014**, *4*, 11121–11123. [[CrossRef](#)]
58. Kim, N.-K.; Min, Y.H.; Noh, S.; Cho, E.; Jeong, G.; Joo, M.; Ahn, S.-W.; Lee, J.S.; Kim, S.; Ihm, K.; et al. Investigation of Thermally Induced Degradation in CH₃NH₃PbI₃ Perovskite Solar Cells using In-situ Synchrotron Radiation Analysis. *Sci. Rep.* **2017**, *7*, 4645. [[CrossRef](#)]
59. Divitini, G.; Cacovich, S.; Matteocci, F.; Cinà, L.; Di Carlo, A.; Ducati, C. In situ observation of heat-induced degradation of perovskite solar cells. *Nat. Energy* **2016**, *1*, 15012. [[CrossRef](#)]
60. Matteocci, F.; Busby, Y.; Pireaux, J.-J.; Divitini, G.; Cacovich, S.; Ducati, C.; Di Carlo, A. Interface and Composition Analysis on Perovskite Solar Cells. *ACS Appl. Mater. Interfaces* **2015**, *7*, 26176–26183. [[CrossRef](#)]
61. Domanski, K.; Correa-Baena, J.-P.; Mine, N.; Nazeeruddin, M.K.; Abate, A.; Saliba, M.; Tress, W.; Hagfeldt, A.; Grätzel, M. Not All That Glitters Is Gold: Metal-Migration-Induced Degradation in Perovskite Solar Cells. *ACS Nano* **2016**, *10*, 6306–6314. [[CrossRef](#)]

